Supporting Information

Regioisomeric Donor-Acceptor-Donor Chromophores Derived from Functionalized Fluorene and Benzo[1,2-*d*:4,5-*d'*]bis([1,2,3]triazole) Units as Potential Organic Laser Materials

Tzu-Chau Lin,*[a] Chen-Yu Chang,[a] Yun-Yi Kao,[a] Shu-Tse Cho,[a] Qian-Wen Guo,[b] Po-Han Chen,[b] Jui-Fen Chang,*[b] Yun-Tzu Tseng,[c] Yuan Jay Chang,*[c] and Wei-Tao Peng*[c]

[a]*Photonic Materials Research Laboratory, Department of Chemistry, National Central University, Jhong-Li District, Taoyuan City 32001, Taiwan. E-mail: tclin@ncu.edu.tw*

[b]*Department of Optics and Photonics, National Central University, Jhong-Li District, Taoyuan City 32001, Taiwan. E-mail: jfchang@dop.ncu.edu.tw*

[c]*Department of Chemistry, Tunghai University, Xitun District, Taichung 40704, Taiwan. E-mail: jaychang@thu.edu.tw & pengwt@thu.edu.tw*

1. Linear optical property measurements

Linear absorption spectra were recorded on a Shimadzu UV-1900i spectrophotometer with freshly prepared samples. The same samples were also used for the measurement of fluorescence spectra and life-time by utilizing a Horiba FluoroMax Plus spectrometer equipped with TCSPC accessories (DeltaPro-DD + NanoLED from Horiba). The aforementioned fluorospectrometer equipped with an integrating sphere (QuantaPhi-2 from Horiba; diameter = 121 mm) was also employed to measure the absolute photoluminescence quantum yield (PLQY) of each model compound in different phases at room temperature;[1] Coumarin 153 (Φ_F = 0.38 ± 5% at λ_{exc} = 423 nm) was used as the standard for the calibration of the integrating sphere and the instrument.[2]

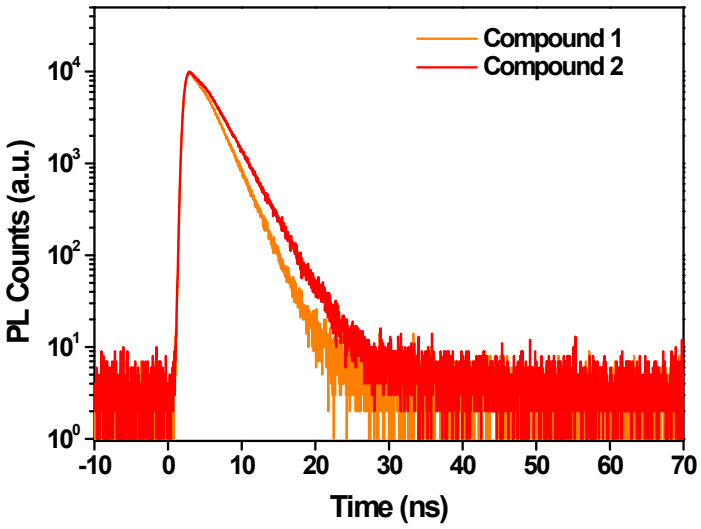

Figure S1. Time-dependent transient PL decay curves of compounds **1** and **2** in toluene.

2. Cyclic voltammetry (CV)

Redox potentials were measured through cyclic voltammetry (CV) by a Zahner Ennium electrochemical analyzer (ZENNIUM X). After purging the samples with nitrogen for 10 minutes under ambient conditions, cyclic voltammetry was conducted in a 10^{-3} M in CH_2Cl_2 solution containing 0.1 M tetrabutylammonium hexafluorophosphate ($TBAPF_6$) as the supporting electrolyte. A conventional three-electrode configuration was used, consisting of a glassy carbon working electrode, a platinum counter electrode, and an Ag/Ag^+ reference electrode.

Table S1. Electrochemical parameters of the studied model compounds.

Compound	E_{ox}[a] (V)	HOMO[b] (eV)	LUMO[c] (eV)
1	0.59	-5.19	-2.79
2	0.51	-5.04	-2.86

[a] Oxidation potential in CH_2Cl_2 (10^{-3} M) containing 0.1 M (n-$C_4H_9)_4NPF_6$ with a scan rate 100 mV·s^{-1}. [b] The HOMO energy level was calculated using the equation: HOMO = -($E_{ox}^{1/2}$-$E_{ox}^{1/2}$(Fc)+4.8), and where $E_{ox}^{1/2}$(Fc) is 0.25 V. [c]The LUMO energy level was calculated by analyzing the relation between E_{HOMO} and ΔE_g^{opt}.

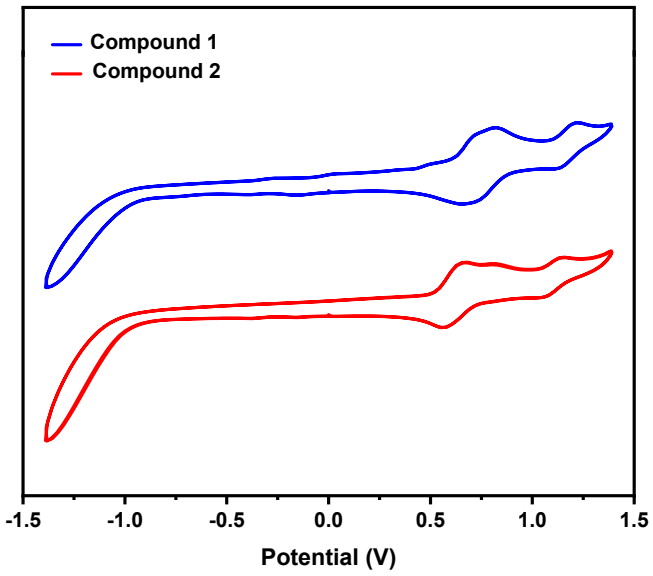

Figure S2 Oxidative voltammograms of compounds **1** and **2**.

3. Theoretical method

Density functional theory (DFT) calculations at the B3LYP/6-31G(d,p)[3] level of theory were performed to determine the electronic and molecular structures of compounds **1** and **2**. The long side chains were truncated and replaced with methyl groups for computational efficiency. This simplification was implemented with the expectation that it would not significantly perturb the properties of the core structures. To validate the simplification, a comparison of the calculated geometries, energetics and corresponding properties for compounds **1** and **2** bearing both full side chains (-C_6H_{13}) and methyl groups (-CH_3) was conducted in Table S2. The good agreement in

geometries and properties between the full-chain and methyl-substituted analogs of **1** and **2** justified the structural simplification for subsequent calculations. To facilitate comparison with experimental absorption and emission spectra, time-dependent DFT (TD-DFT)[4] calculations were performed at TD-B3LYP/6-31G(d,p) level on the optimized geometries of the ground and first excited states of both compounds. Furthermore, the polarizable continuum model with the integral equation formalism (IEFPCM) method on the gas-phase optimized geometries, with a dielectric constant of toluene, has been applied to simulate the solvent effects. Table S3 presents a comparison of the gas-phase and solution-phase results, demonstrating the good agreement between the two computational approaches for these systems. For direct correlation with experimental data, the discussion section utilize the excitation energies from the solution-phase results. All calculations were performed with the Gaussian 16 package.[5] The HOMO and LUMO molecular orbitals were generated using GaussView 6.

Table S2. The comparison of the computed torsional angles, energetics, and properties for **1** and **2** with full side chains (full) and methyl groups (-CH_3) substitutions. All calculations were performed at the B3LYP/6-31G(d,p) level of theory for the ground state geometry in the gas phase. The torsional angles represent the two dihedral angles between the central BBTA core and the fluorene groups on each side. The HOMO and LUMO energies are reported for the ground state. Absorption energies (E_{abs} in eV) for the first excited state of **1** and **2**, and their corresponding oscillator strength (*f*) were computed using the TD-B3LYP/6-31G(d,p)//B3LYP/6-31G(d,p) level of theory. Solvent effects were included using the IEFPCM method (solvent = toluene) on geometries optimized at the ground state in the gas phase. All excited states calculated here are predominantly HOMO to LUMO transitions (>98%).

		torsional angles	**HOMO (eV)**	**LUMO (eV)**	E_{abs} **(eV)**	***f***
1	full	27°/54°	-4.665	-1.983	2.375	0.986
	(in toluene)	---	(-4.782)	(-2.118)	(2.319)	(1.141)
	-CH_3	26°/54°	-4.670	-2.032	2.337	1.026
	(in toluene)	---	(-4.777)	(-2.152)	(2.281)	(1.184)
2	full	26°/26°	-4.502	-2.167	2.079	1.246
	(in toluene)	---	(-4.622)	(-2.285)	(2.022)	(1.411)
	-CH_3	26°/26°	-4.527	-2.219	2.057	1.248
	(in toluene)	---	(-4.643)	(-2.323)	(2.008)	(1.417)

Table S3. Computed excitation energies of the lowest-energy electronic excitations from the optimized structures of ground and first excited states (E_{abs} and E_{PL} in eV, respectively), and oscillator strengths (f) for (methyl-substituted) **1** and **2**, with and without solvent effects. Solvent effects were included using the IEFPCM method (solvent=toluene) on geometries optimized at the ground state in the gas phase. All excited states calculated here are predominantly HOMO to LUMO transitions (>98%).

		E_{abs} (eV)	f	E_{PL} (eV)	f
1	Gas	2.337	1.026	1.967	1.328
	In toluene	2.281	1.184	1.891	1.505
2	Gas	2.057	1.248	1.717	1.361
	In toluene	2.008	1.417	1.652	1.554

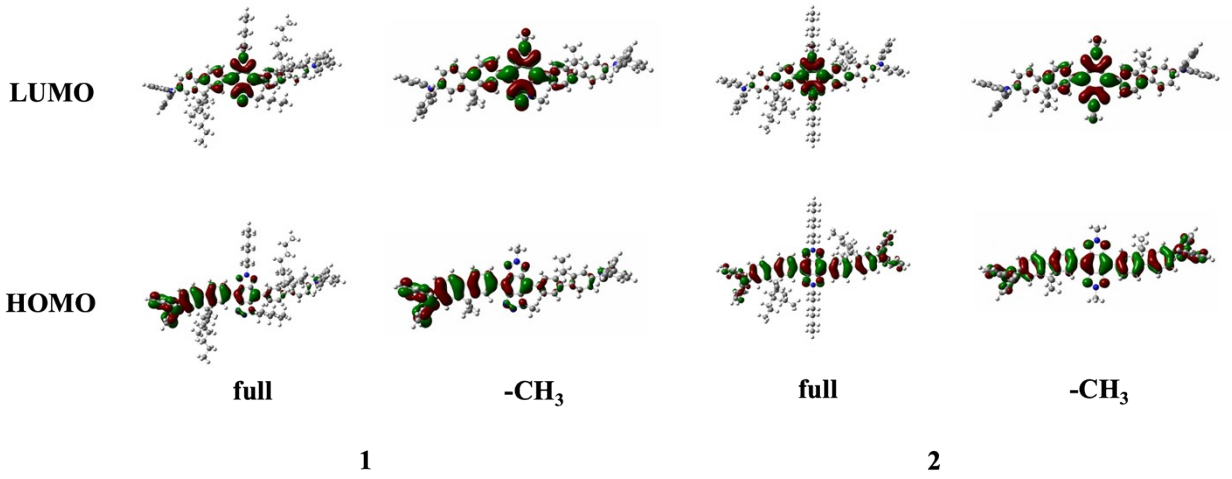

Figure S3. HOMO and LUMO distributions for compounds **1** and **2** without (full) and with (-CH_3) methyl replacement for the side chains calculated at the B3LYP/6-31G(d,p) level of theory.

4. Film fabrication

Neat films were spin-coated from a tetrahydrofuran (THF) solution (12 mg/mL) at 700 rpm to achieve a controlled thickness of approximately 200 nm. On the other hand, doped films were prepared using poly(9,9-di-*n*-octylfluorenyl-2,7-diyl) (**PFO**) and **2DFL-Tr2** (*i.e.* it was assigned as compound **2** in ref. 13 of the body text and the molecular structure of this chromophore is shown in Figure S4) as the host materials for **1** and **2**, respectively, with a doping ratio of 4 wt %. The host and guest materials were co-dissolved in THF at concentrations of 12 mg/mL and 0.48 mg/mL, respectively. The solution was then deposited at a rotation speed of 800-1000 rpm to achieve the film thickness of approximately 200 nm. The film thickness was characterized using a surface profilometer, with a measurement uncertainty of ±10 nm. Macroscopic thickness profiling revealed that the film exhibits a maximum thickness of approximately 200 nm at its center, gradually

decreasing by about 20 nm toward peripheral regions located 5 mm from the center. Accordingly, ASE measurements were conducted in the central region, where the film thickness is most uniform and no significant variation in ASE threshold was observed. For ASE characterization, the sample was carefully cleaved from this central region to produce a well-defined edge, enabling efficient edge-emission collection.

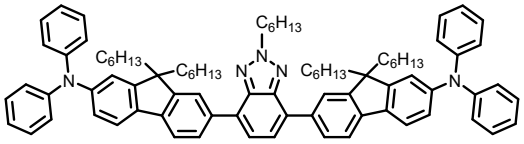

Figure S4. The molecular structure of **2DFL-Tr2**.

The spectral overlap of each host-guest compound set used in this part of experiment as well as the comparison of the photoluminescence spectra of the fabricated neat-films and doped-films based on the corresponding host and guest compounds are presented in Figure S5.

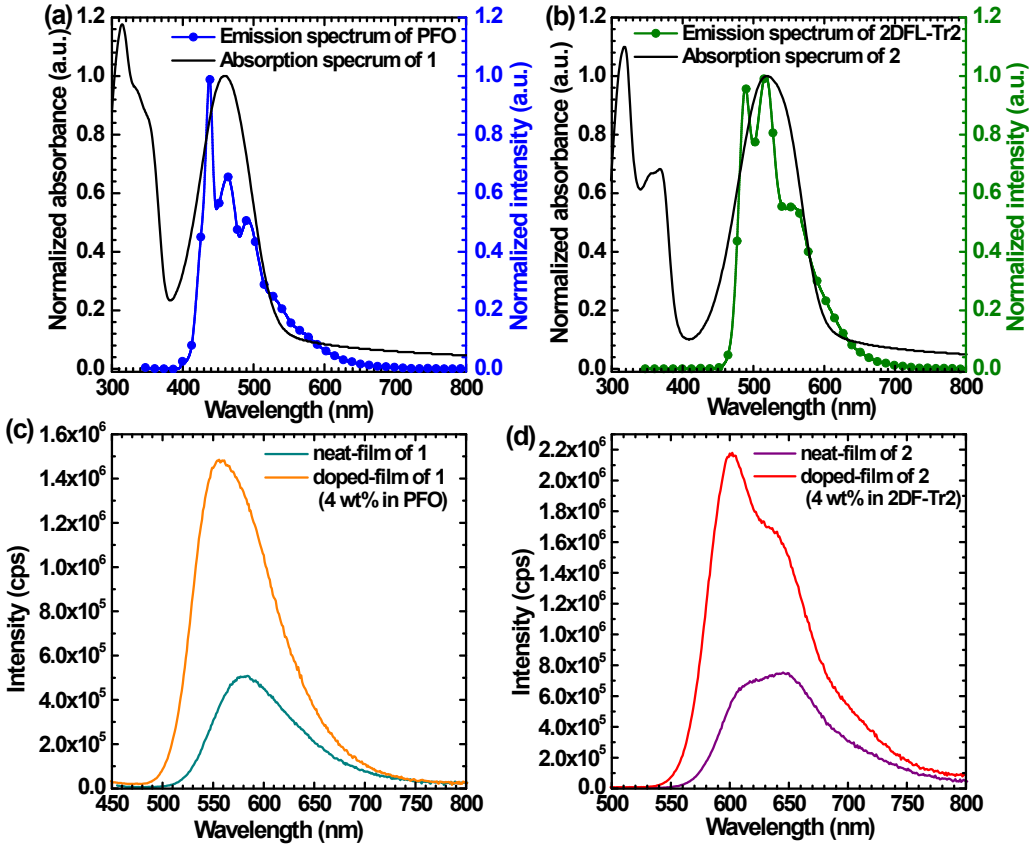

Figure S5. The spectral overlap between the selected host and the corresponding guest compounds in their neat-film state: (a) normalized emission spectrum of PFO vs. normalized absorption spectrum of compound **1**, and (b) normalized emission spectrum of **2DFL-Tr2** vs. normalized absorption spectrum of compound **2**. (c) and (d) are the emission spectra of the fabricated neat-films based on **1** and **2** and doped-films based on the indicated corresponding components.

From Figures S5(a) and S5(b), it is noted that there is certain extent of the spectral overlap between normalized emission and absorption spectra of the neat-films made of the corresponding host-guest compound set, which fulfills the prerequisite for the occurrence of Förster resonance energy transfer between the host and guest molecules in doped-film configuration. Moreover, it is experimentally found that the doping ratio of 4 wt% can lead to the largest enhancement of PL in this studied system. As shown in Figures S5(c) and S5(d), both doped-films exhibit over twofold enhanced PL intensity compared to that of the corresponding neat-films and such a feature has verified the occurrence of Förster resonance energy transfer in these host-guest systems.

5. Amplified spontaneous emission (ASE) related measurements

● Samples in solution phase

The experimental setup for the ASE characterization measurements for solution samples is illustrated in Figure S6. A nitrogen laser (NL100, SRS) with a central wavelength at 337.1 nm was served as the excitation source to provide laser pulses with a repetition rate of 10 Hz and a pulse duration of 3.5 ns. The pump energy was regulated by a motorized variable ND-filter and the laser beam was focused onto the front-surface of the cuvette filled with the studied dye solution (1×10^{-3} M in toluene) to form a line stripe (1 cm in length) using a combination of a tunable slit and a cylindrical lens (f = 10 cm). The side-emission from the cuvette was collected through an optical fiber and analyzed by a CCD spectrometer (QE-Pro, Ocean Optics).

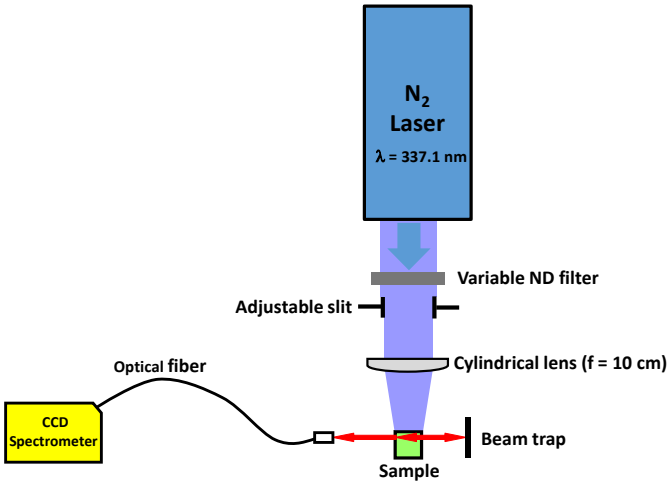

Figure S6. ASE characterization setup for solution samples.

● Samples in film phase

Figure S7 illustrates the schematic of the ASE measurement system for film samples, constructed in ambient atmosphere. A frequency-tripled 355 nm Nd:YAG nanosecond pulsed laser (Q-smart 450, Quantel Laser) with linewidth <0.005 cm^{-1} and a 10 Hz repetition rate was employed as the pumping source. A motorized attenuator (Watt Pilot, Altechna) was used to adjust the laser energy. Lens 1 (f_1

= 7.5 cm) and lens 2 (f_2 = 15 cm), separated by the sum of their focal lengths, formed an afocal system that expanded the laser beam size to approximately 8 mm in diameter. A cylindrical lens (f = 10 cm) then focused the laser beam one-dimensionally into a narrow stripe width of W = 271 μm, incident on the sample positioned at the back focal plane. An adjustable mechanical slit, placed between the cylindrical lens and the sample, filtered out the outer regions of the less intense laser beam and defined the length of the focused laser beam (L = 3 mm) incident on the edge of the sample. This ensures a uniform intensity distribution of laser excitation on the sample, with an area of $A = W \times L = 8.13\times10^5\ \mu m^2$. The ASE from the sample was collected by a collimating lens, aligned with the edge of sample in the off-axis direction, and coupled to an optical fiber connected with a spectrometer (HR4000, Ocean Optics). Before and after the ASE measurements, the incident laser power at the sample position was recalibrated using a high-sensitivity thermal sensor (Ophir, model 3A-PF-12) to ensure laser stability throughout the measurement process. The pulse-to-pulse energy fluctuation was measured to be less than 10%, and the average laser power remained relatively stable over the duration of several hours, exhibiting a variation of less than 10%.

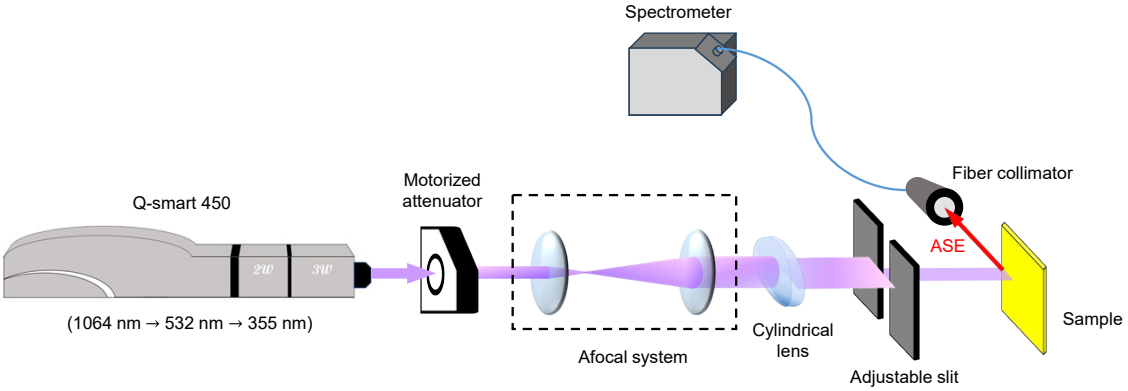

Figure S7. ASE experiments setup for film samples.

● Determination criteria of ASE thresholds

In the input-output intensity plot, the data corresponding to regions below and above the onset of ASE were individually fitted using linear regressions optimized to minimize the root-mean-square error. The ASE threshold is determined as the excitation power at which a change in slope occurs. This inflection point marks the transition from the regime dominated by spontaneous emission to the regime where ASE prevails.[6]

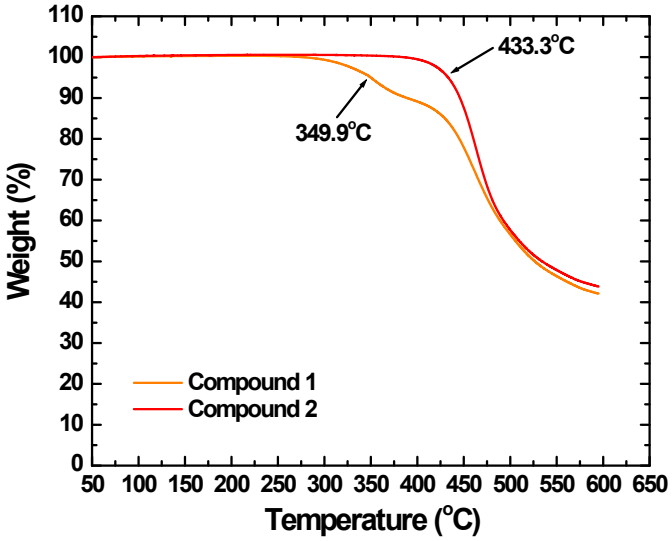

Figure S8. Measured TGA curves of compounds **1** and **2** under nitrogen atmosphere.

6. Photostability test

The photostability of compounds **1** and **2** was tentatively evaluated in their solution and neat-film phases under air-exposure condition using the optical setups illustrated in Figure S6 and Figure S7 , respectively. The solution samples were freshly prepared in toluene at concentration of 1×10^{-3}M and the film samples were prepared through the same method described in the preceding section.

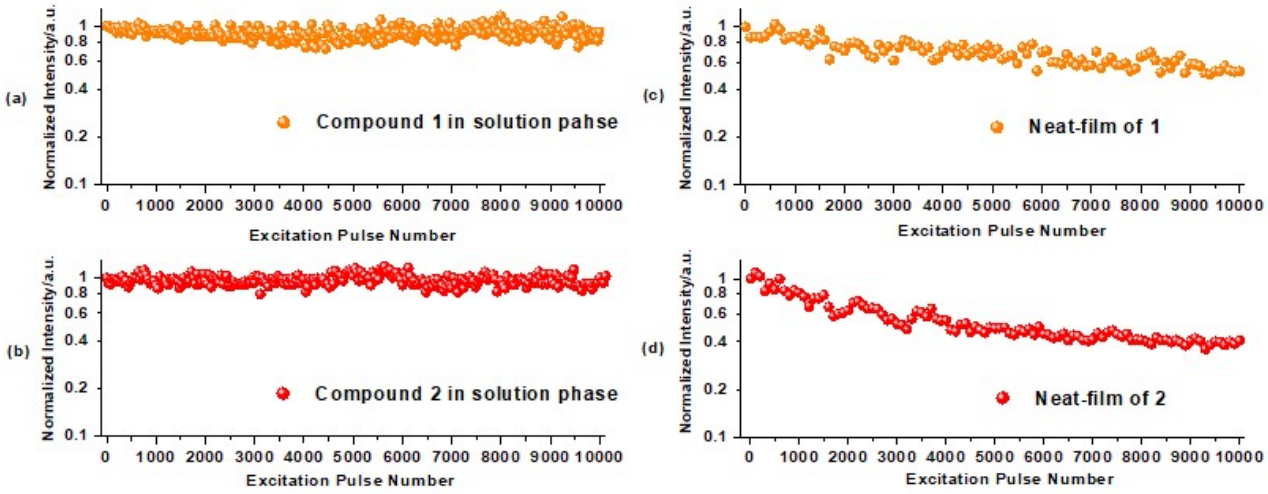

Figure S9. The evolution of ASE peak intensity of compounds **1** and **2** in solution ((a) & (b)) and neat-film ((c) & (d)) states at optical pumping intensity of twice their ASE thresholds.

7. Numbering of C and H of the precursors and final chromophores for NMR assignment

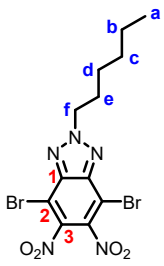

4

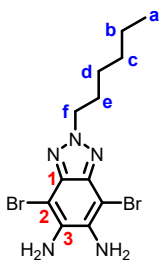

5

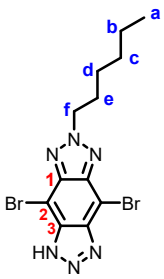

6

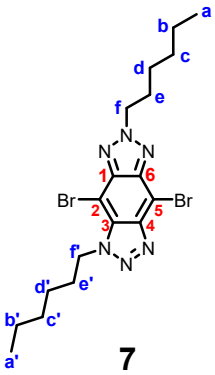

7

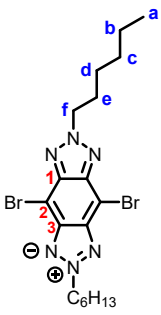

8

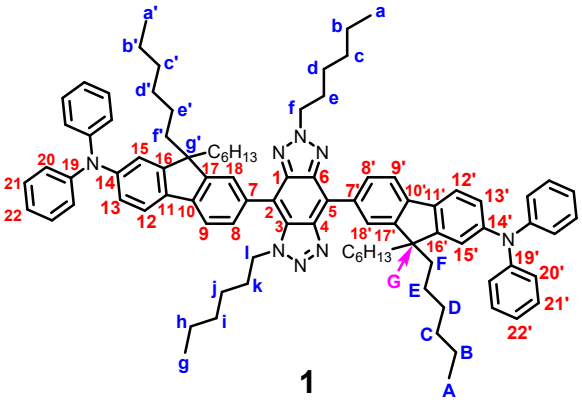

1

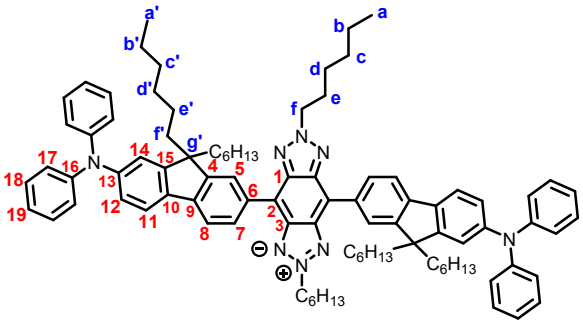

2

8. ^{1}H and ^{13}C NMR spectra of the precursors and final compounds

^{1}H NMR Spectrum of Compound **4**

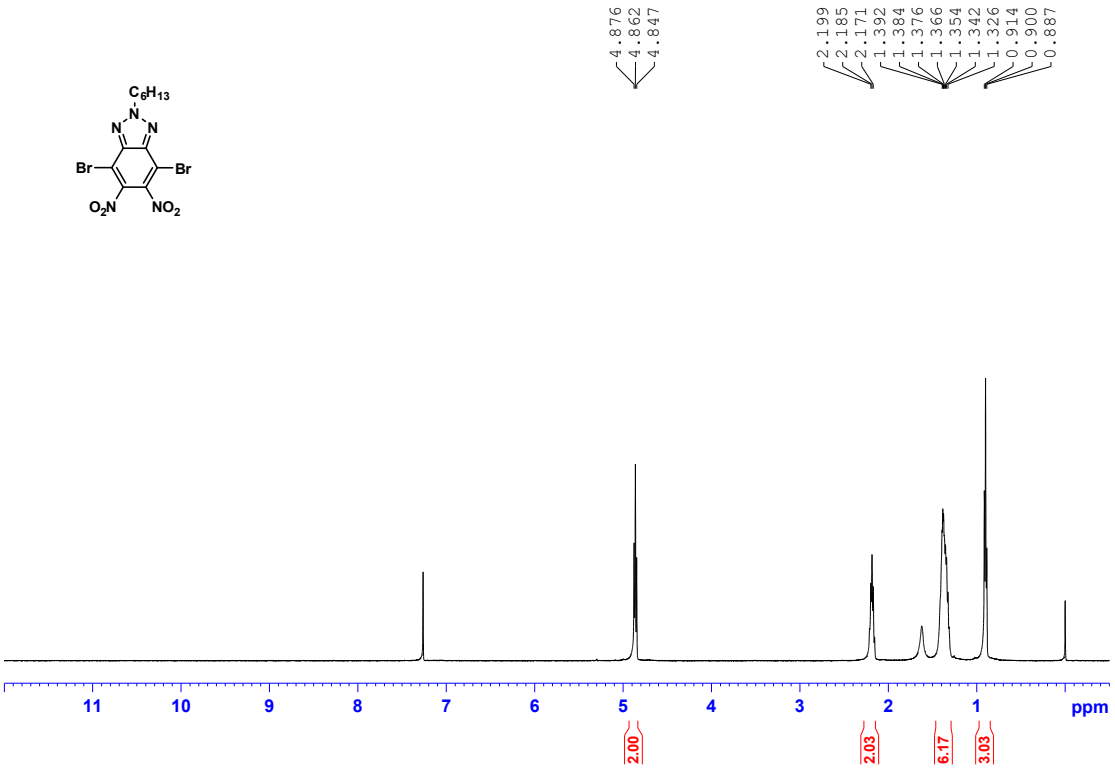

^{13}C NMR Spectrum of Compound **4**

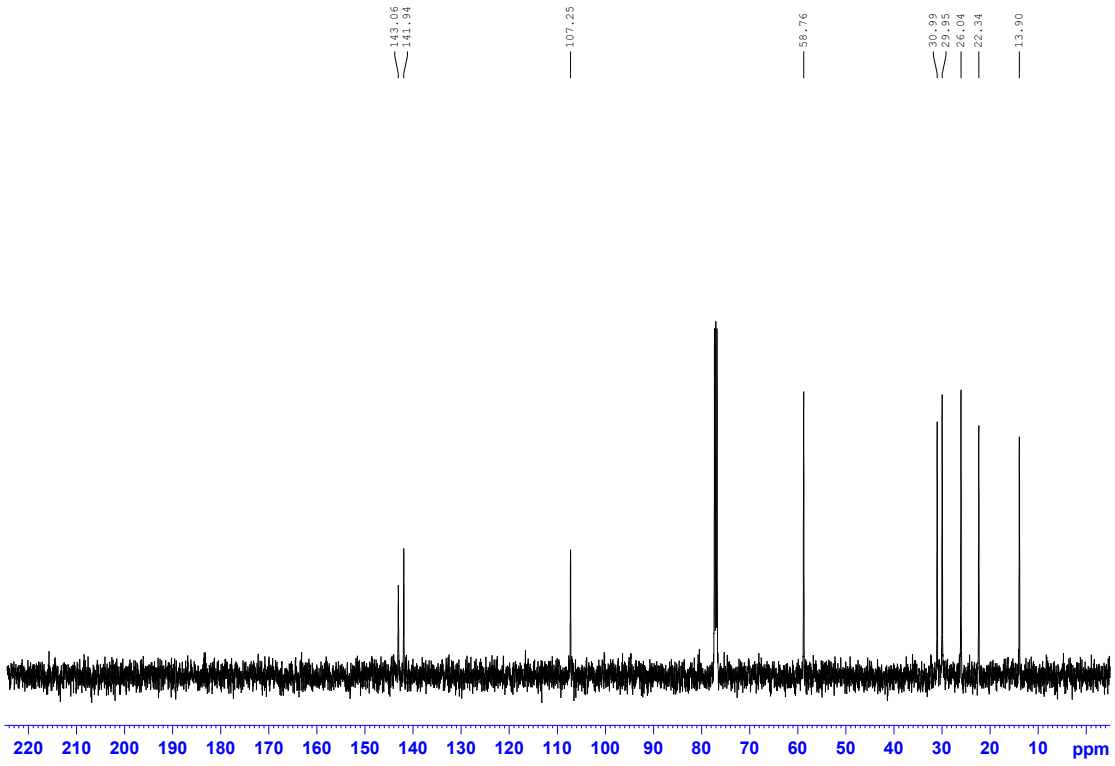

^{1}H NMR Spectrum of Compound **5**

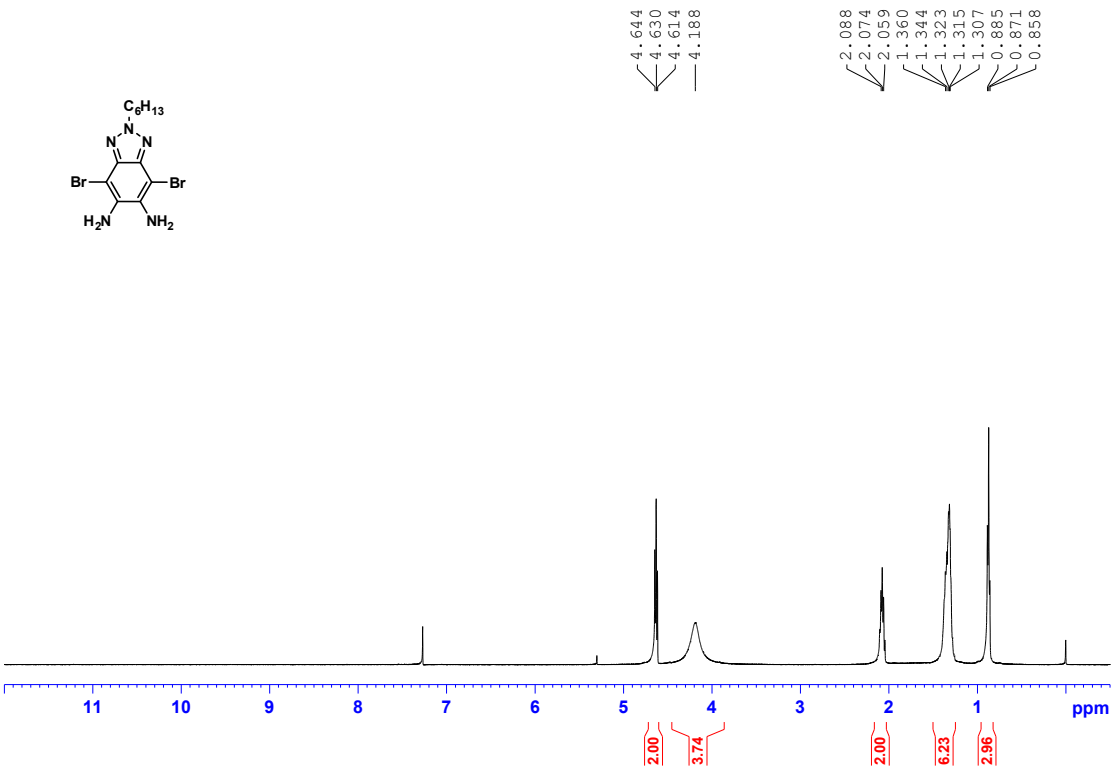

^{13}C NMR Spectrum of Compound **5**

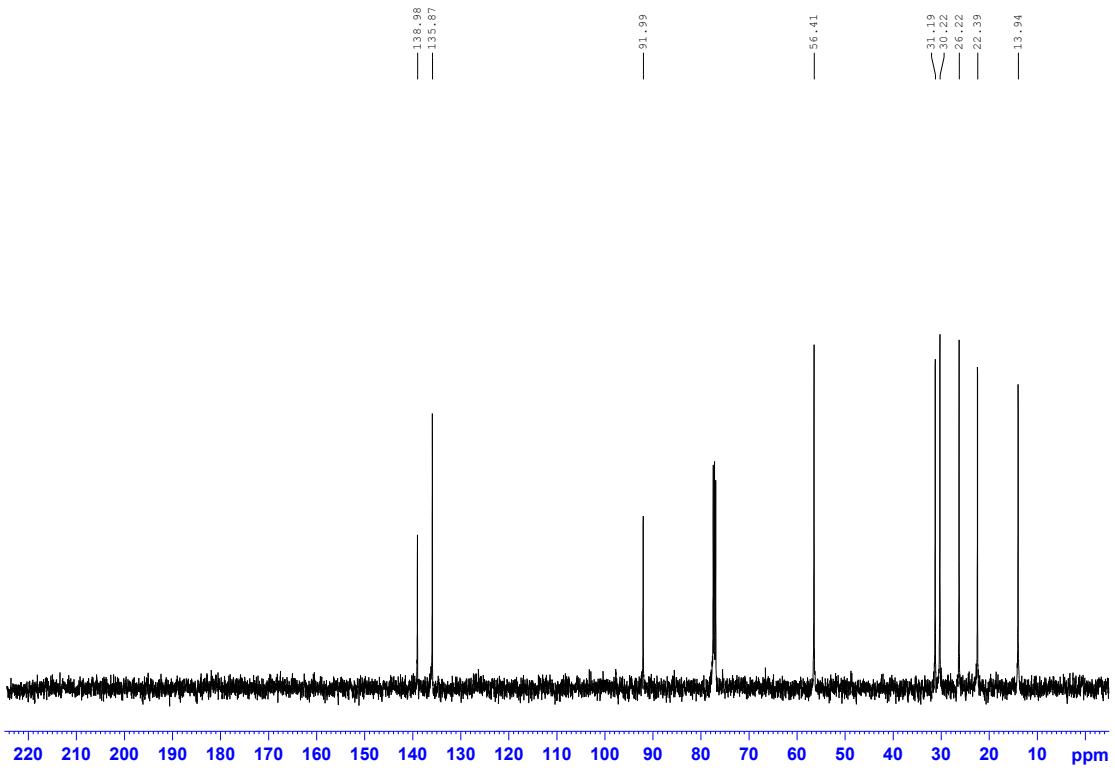

^{1}H NMR Spectrum of Compound **6**

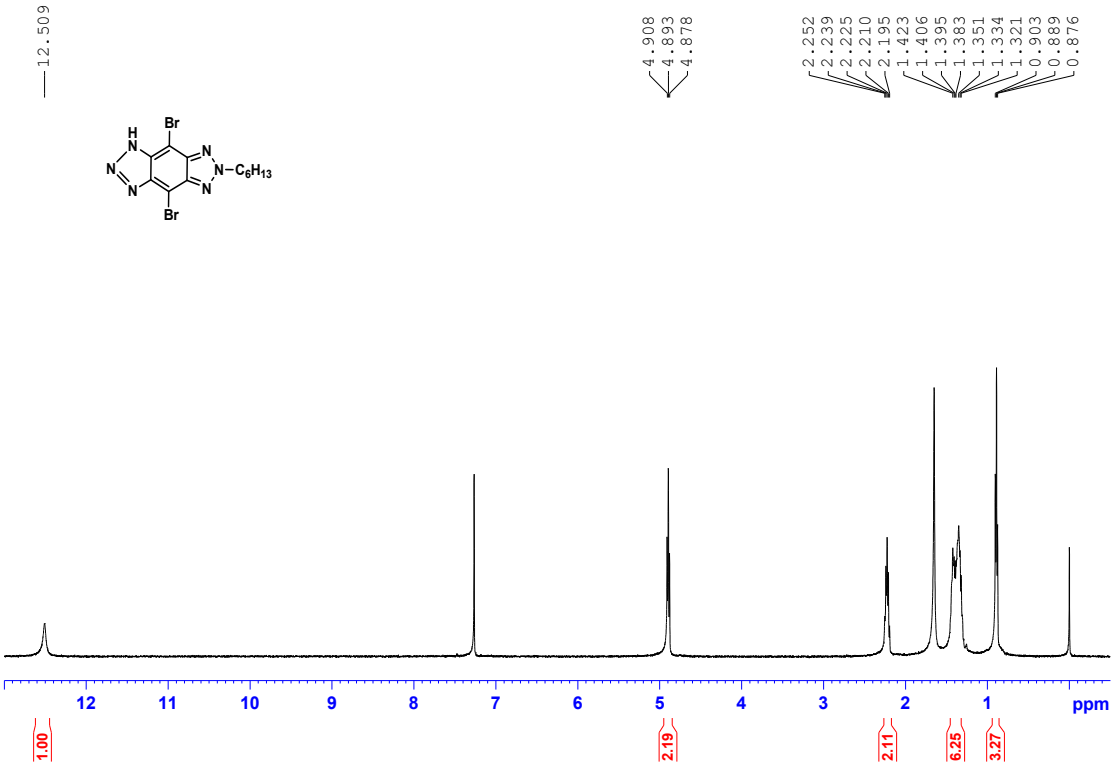

^{13}C NMR Spectrum of Compound **6**

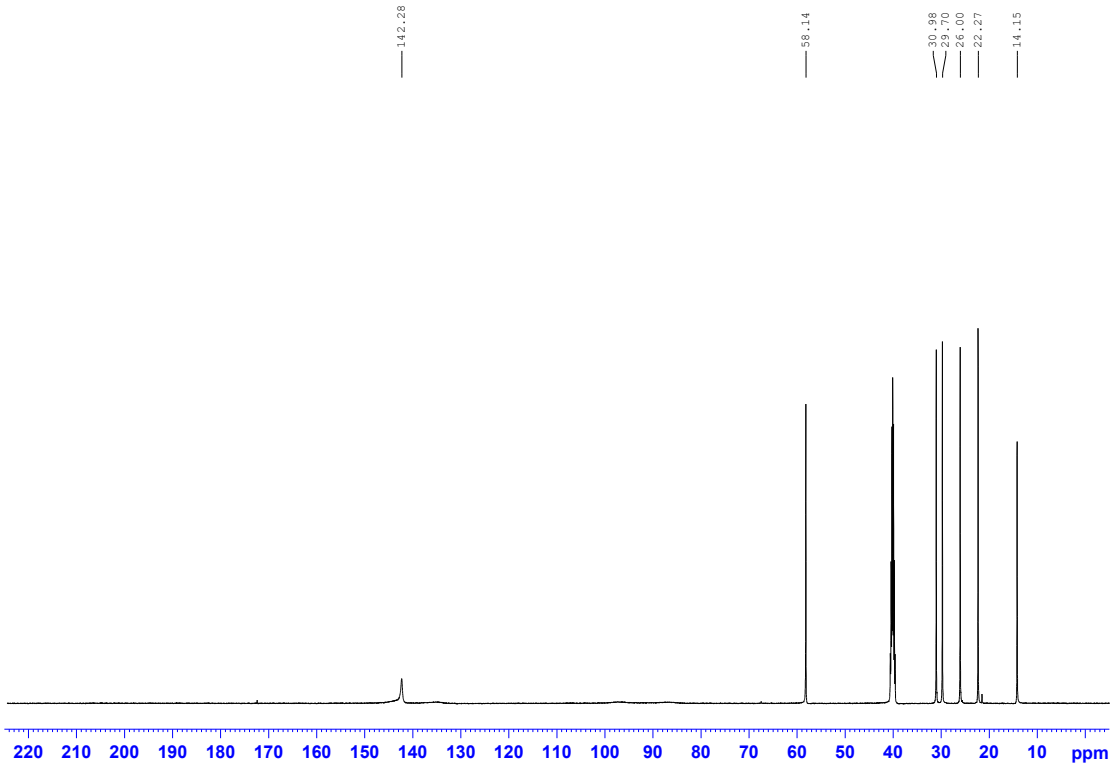

^{1}H NMR Spectrum of Compound **7**

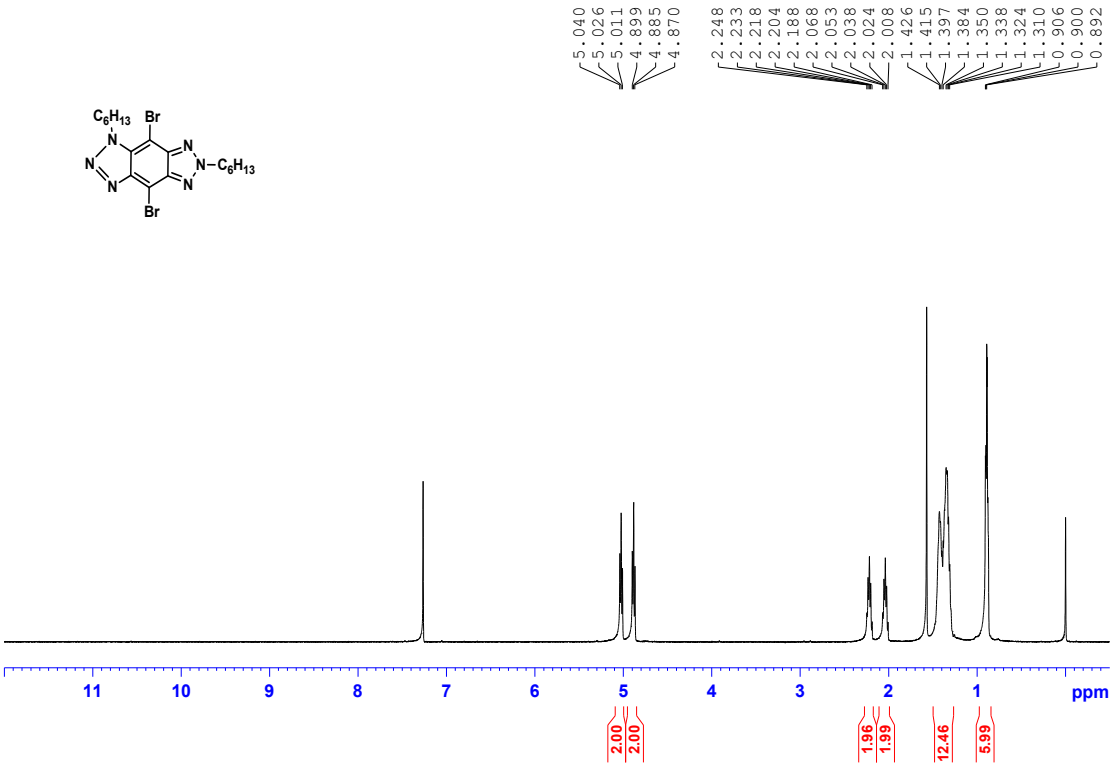

^{13}C NMR Spectrum of Compound **7**

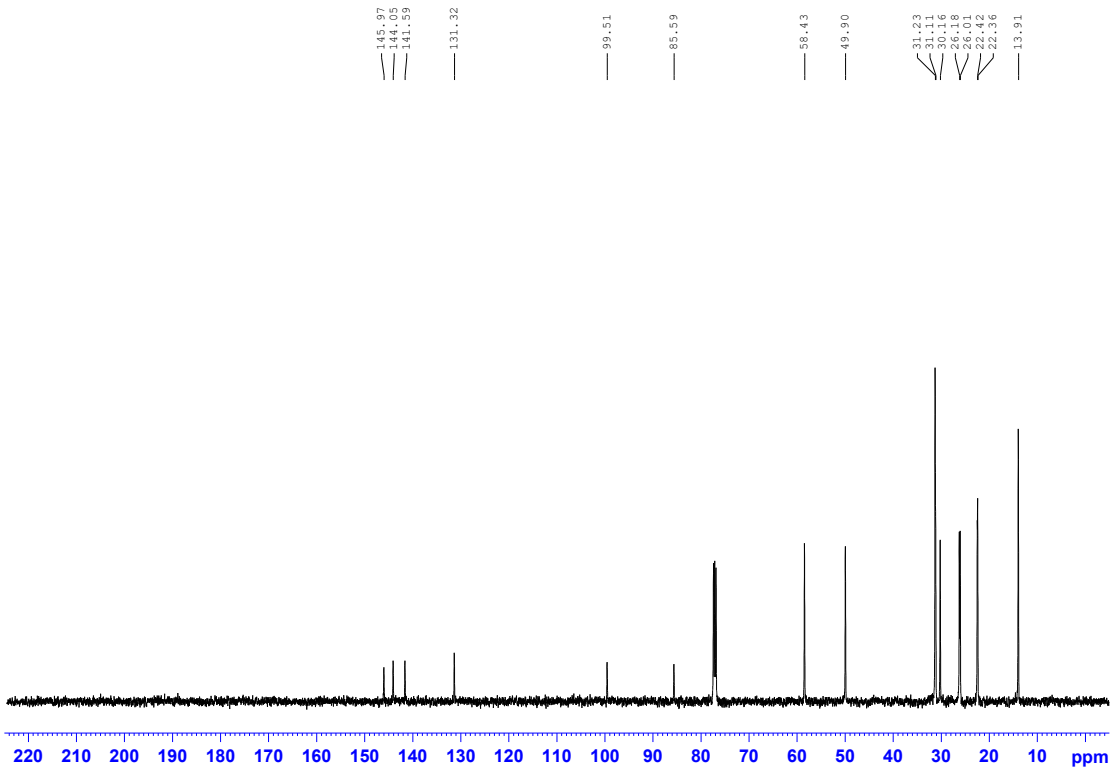

[1]H NMR Spectrum of Compound **8**

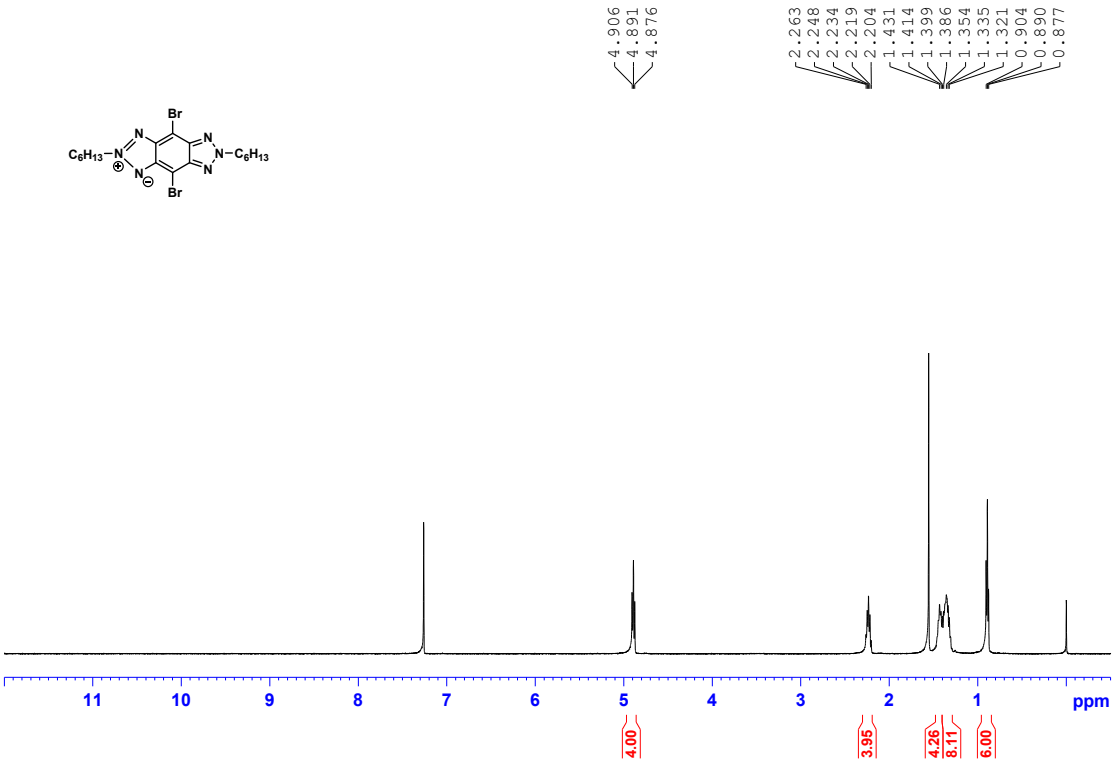

[13]C NMR Spectrum of Compound **8**

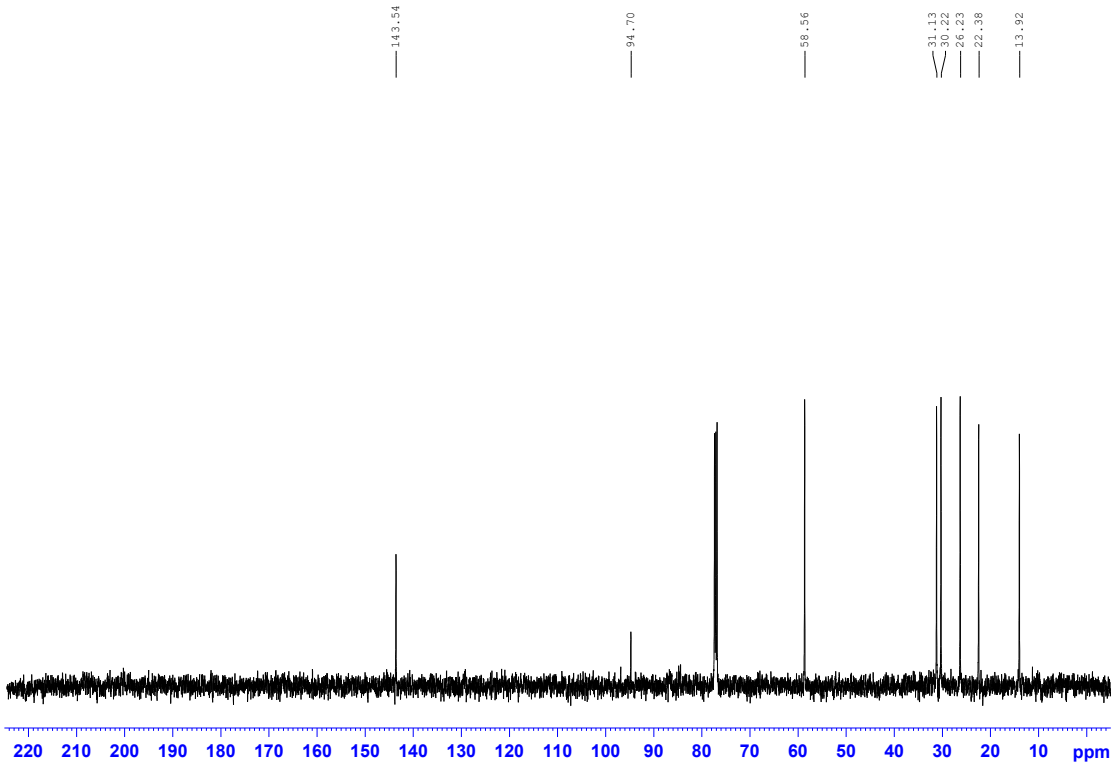

^{1}H NMR Spectrum of Compound **1**

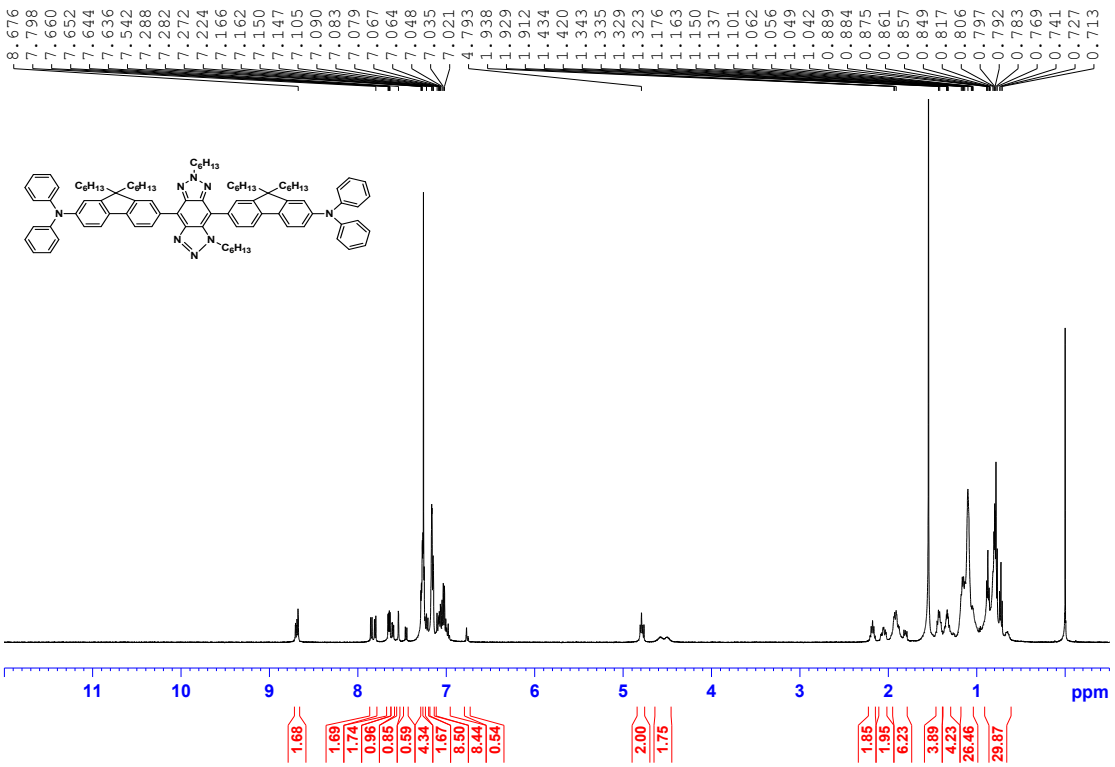

^{13}C NMR Spectrum of Compound **1**

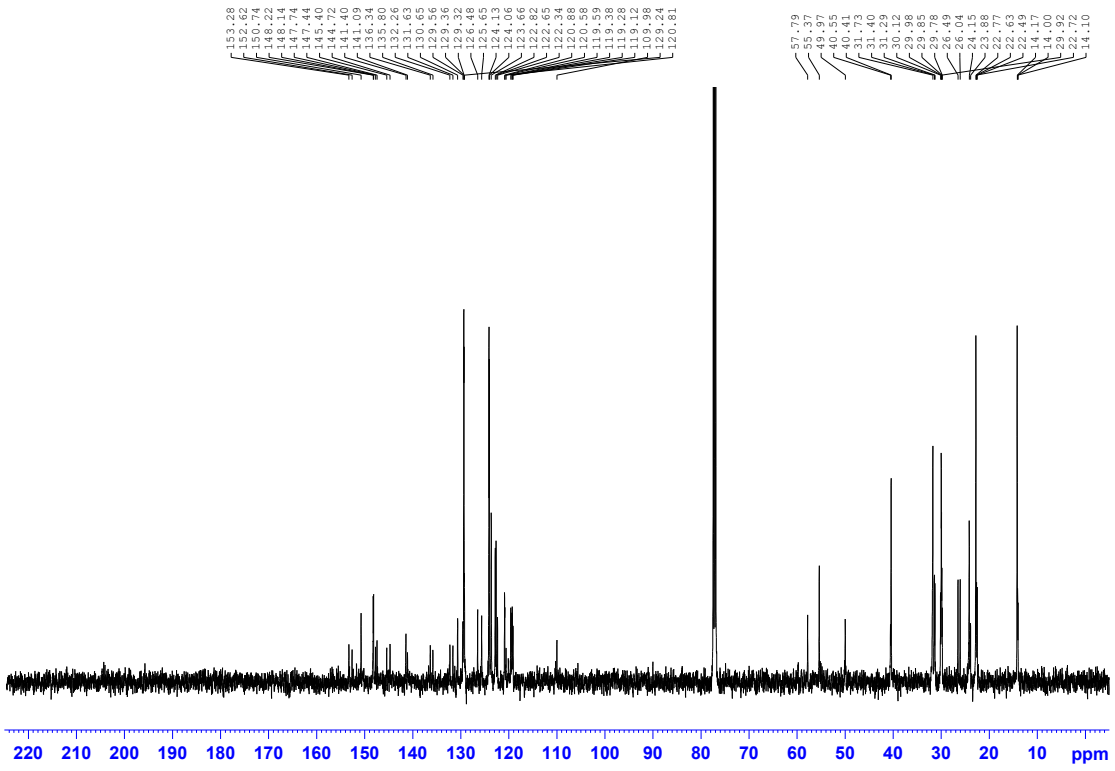

^{1}H NMR Spectrum of Compound **2**

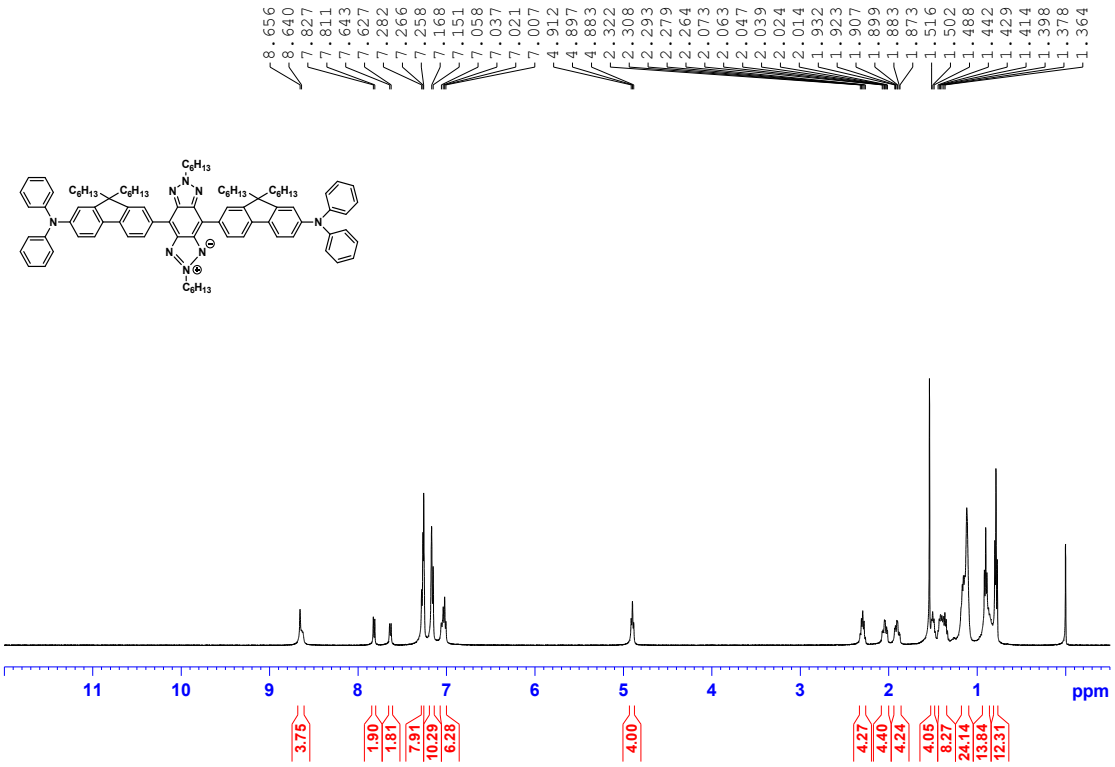

^{13}C NMR Spectrum of Compound **2**

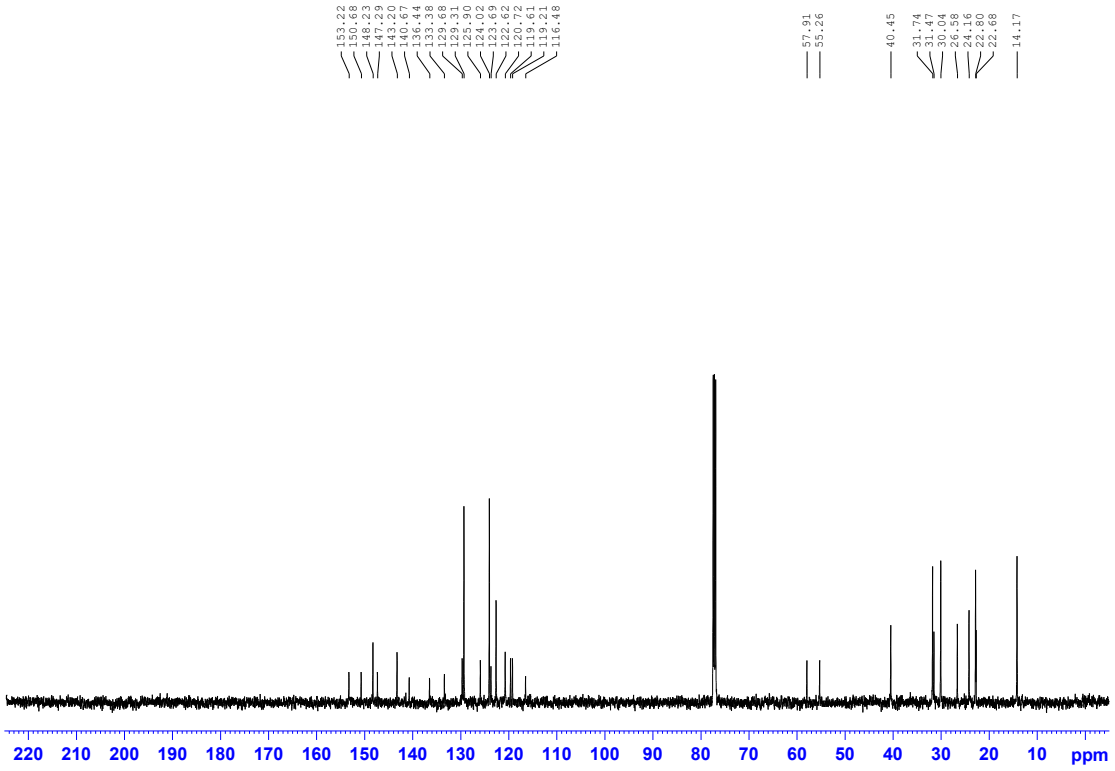

References

[1] L. Porres, A. Holland, L.-O. Palsson, A. P. Monkman, C. Kemp and A. Beeby, *J. Fluoresc.* **2006**, *16*, 267-273.

[2] (a) J. A. Gardecki and M. Maroncelli, *Applied Spectroscopy* **1998**, *52*, 1179-1189; (b) G. A. Reynolds and K. H. Drexhage, *Optics Communications* **1975**, *13*, 222-225.

[3] (a) A.D. Becke, *J. Chem. Phys*. **1993**, 98, 5648-5652; (b) C. Lee, W. Yang, R.G. Parr, *Phys. Rev. B* **1988**, 37, 785-789; (c) S.H. Vosko, L. Wilk, M. Nusair, Can. *J. Phys*. **1980**, 58, 1200-1211; (d) P.J. Stephens, F.J. Devlin, C.F. Chabalowski, M.J. Frisch, *J. Phys. Chem*. **1994**, 98, 11623-11627.

[4] R.E. Stratmann, G.E. Scuseria, M.J. Frisch, *J. Chem. Phys*. **1998**, 109, 8218-8224.

[5] M. J. Frisch, G. W. Trucks, H. B. Schlegel, G. E. Scuseria, M. A. Robb, J. R. Cheeseman, G. Scalmani, V. Barone, G. A. Petersson, H. Nakatsuji, X. Li, M. Caricato, A. V. Marenich, J. Bloino, B. G. Janesko, R. Gomperts, B. Mennucci, H. P. Hratchian, J. V. Ortiz, A. F. Izmaylov, J. L. Sonnenberg, Williams, F. Ding, F. Lipparini, F. Egidi, J. Goings, B. Peng, A. Petrone, T. Henderson, D. Ranasinghe, V. G. Zakrzewski, J. Gao, N. Rega, G. Zheng, W. Liang, M. Hada, M. Ehara, K. Toyota, R. Fukuda, J. Hasegawa, M. Ishida, T. Nakajima, Y. Honda, O. Kitao, H. Nakai, T. Vreven, K. Throssell, J. A. Montgomery Jr., J. E. Peralta, F. Ogliaro, M. J. Bearpark, J. J. Heyd, E. N. Brothers, K. N. Kudin, V. N. Staroverov, T. A. Keith, R. Kobayashi, J. Normand, K. Raghavachari, A. P. Rendell, J. C. Burant, S. S. Iyengar, J. Tomasi, M. Cossi, J. M. Millam, M. Klene, C. Adamo, R. Cammi, J. W. Ochterski, R. L. Martin, K. Morokuma, O. Farkas, J. B. Foresman, D. J. Fox, Wallingford, CT 2016.

[6] K. L. Shaklee and R. F. Leheny, *Appl*. *Phys*. *Lett*., **1971**, *18*, 475-477; (b) S. Milanese, M. L. De Giorgi, L. Cerdán, M. G. La-Placa, P. P. Boix, H. J. Bolink, and M. Anni, *Materials Today: Proceedings*, **2022**, *67*, 959-963.